Received March 20, 2022, accepted April 2, 2022, date of publication April 7, 2022, date of current version April 14, 2022.

Digital Object Identifier 10.1109/ACCESS.2022.3165562

A Low-Profile Dual-Band Dual-Polarized Quasi-Endfire Phased Array for mmWave 5G Smartphones

MENGLOU RAO, (Graduate Student Member, IEEE), AND KAMAL SARABANDI, (Life Fellow, IEEE)
Radiation Laboratory, Department of Electrical Engineering and Computer Science, University of Michigan, Ann Arbor, MI 48109, USA
Corresponding author: Menglou Rao (menglrao@umich.edu)

ABSTRACT This paper presents a very low-profile ($0.105\lambda_0$ at 28 GHz) dual-band dual-polarized millimeter-wave phased array for 5G smartphones. The array element is based on two distinct dual-band antennas to realize two orthogonal linear polarizations. A planar folded dipole with a parasitic strip is used to produce horizontally polarized radiation, and a novel *hexagonal bridge antenna* is devised to generate vertically polarized radiation while maintaining a very low profile. A prototype of a 1×4 phased array is designed and implemented on a multilayer laminate using standard printed circuit board process. The real estate of the array is kept within 6.5 mm $\times$ 23 mm $\times$ 1.12 mm. For both polarizations, the -10 dB bandwidth covers 25.4–30.84 GHz and 38–40 GHz with peak gains of 11.31 and 11.93 dBi at two center frequencies, respectively. The overlapped 3 dB scan ranges between both polarizations are $\pm 45°$ at 28 GHz and $\pm 39°$ at 39 GHz. This work considers a number of important design challenges of implementing low-cost mmWave antennas in smartphones, providing a practical solution to mmWave 5G mobile devices.

INDEX TERMS 5G, mmWave antenna arrays, antenna miniaturization, vertically polarized radiation, endfire radiation.

I. INTRODUCTION

The world has witnessed the fast rollout of the fifth-generation wireless networks, denoted as 5G, for the past several years. This new wireless network promises to deliver ultra-high data rate, superior reliability and negligible latency. Among numerous enabling technologies for 5G, the deployment of the millimeter-wave (mmWave) spectrum is believed to be the key to make the ultimate performance a reality [1], [2]. Until March 2020, the Federal Communications Commission (FCC) has completed auctions of multiple bands above 24 GHz for 5G uses, including the 24 GHz, the 28 GHz, and the upper 37 GHz, 39 GHz and 47 GHz bands, with a future plan to free up additional spectrum in the 26 GHz and 42 bands, and to make more efficient use of the 70/80/90 GHz bands [3]. Since spectrum harmonization cross regions is limited, it is favorable to have antennas that feature wideband performance and can simultaneously cover multiple 5G frequency bands to meet different standards around the world.

The associate editor coordinating the review of this manuscript and approving it for publication was Debdeep Sarkar.

In addition, mmWave 5G antennas for mobile devices must feature polarization diversity in order to cope with unpredictable mobile channel environments. It is experimentally demonstrated that the polarization mismatch becomes a substantial loss factor that heavily affects the overall quality of the wireless link at mmWave frequencies, and dual-polarized phased arrays can provide more reliable Quality of Service (QoS) for mmWave 5G mobile phones than their single-polarized counterparts [4], [5]. Recently, several dual-band dual-polarized mmWave antennas have been proposed for 5G applications [6]–[12]. These designs use either stacked patches [6]–[11] or planar dipoles [12]. However, their height profiles are in the range of $2-4$ mm, whereas the typical thickness of the printed circuit boards (PCBs) used in cell phones is around 1 mm. The large sizes of the antennas make them impractical for 5G smartphones. A recently developed patch array with a multilayer reactive impedance surface (RIS) [11] achieves a bandwidth of 26.22–29.57 GHz on a 1.122 mm thick substrate. A major issue with patch antennas is that they inherently exhibit broadside radiation with sub-hemispherical coverage. Consider the use case scenario

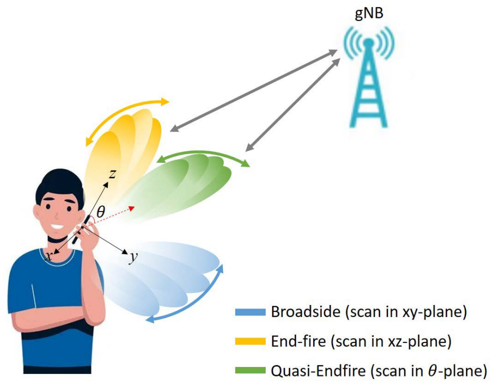

FIGURE 1. Beam coverage of different antenna configurations.

FIGURE 2. PCB stack-up.

depicted in Fig. 1 where the user is holding the cell phone with the antenna plane facing downwards. In this case, a broadside array alone cannot establish a reliable communication link with the gNB base station.

Endfire antennas can effectively complement broadside arrays and have been investigated in the past few years [5], [13]–[18]. While horizontally polarized radiation in the endfire direction can be realized with relative ease using a planar dipole structure, exciting a vertically polarized electric field within a very thin substrate is extremely challenging. Despite substantial research efforts that have been put into mmWave 5G antennas, only a few low-profile dual-polarized endfire antennas suitable for smartphones have been reported [5], [14]. In [5], a dual-polarized endfire array with a total height of 0.52 mm is designed for 60 GHz applications. In [14], two types of Yagi-Uda antennas are designed on a 10-layer FR-4 laminate with a total height of 0.8 mm. However, the antennas can only cover a small portion of the 28 GHz band. Sometimes stringent design constraints, such as large metallic displays closely below the antennas, make it almost impossible to create perfect endfire radiation. In this case, antenna arrays with quasi-endfire radiation can be considered alternatives as they are still able to establish a connection with the base station as demonstrated in Fig. 1. So far, very few dual-band dual-polarized endfire or quasi-endfire [19] mmWave 5G antennas for smartphones are available in the literature. In [19], the gain of the vertically polarized antenna in the endfire direction is highly dependent on the substrate thickness, thus it cannot provide satisfying performance for thin smartphones.

Focusing on the design challenges mentioned above, this paper proposes a very compact dual-band dual-polarized array that can simultaneously cover the 28 GHz and the 39 GHz bands for mmWave 5G smartphones. The array element is based on two individual antennas, a planar folded dipole and a novel *hexagonal bridge antenna*, which respectively provide endfire horizontally polarized radiation and quasi-endfire vertically polarized radiation. The array element features lateral dimensions of 6.5 mm × 5 mm and a height profile of only 1.12 mm. A prototype of a 1 × 4 phased array is designed, fabricated and tested. The size of the array is 6.5 mm × 23 mm × 1.12 mm ($0.607\lambda_0 \times 2.147\lambda_0 \times 0.105\lambda_0$, where λ_0 is the free-space wavelength at 28 GHz), which is suitable for cellular applications. The array is intended to be incorporated along the edges of a mobile phone for beam steering.

The rest of the paper is organized as follows: Section II provides the design detail of the array element. In Section III, advanced measurement techniques are used to characterize the antennas. Section IV presents the 1 × 4 array topology. Basic performance metrics and scanning capability of the array are experimentally investigated, and are compared with some recently published dual-band dual-polarized antenna arrays. Section V concludes the paper.

II. ARRAY ELEMENT DESIGN

This section presents the design detail of the proposed dual-band dual-polarized antenna. The targeted bandwidth is 26–30 GHz and 38 GHz–40 GHz. A pair of extremely low-profile antennas are devised to produce two orthogonal polarizations. The design is realized on a multilayer RO 4003C ($\epsilon_r = 3.55, \tan\delta = 0.0027$) laminate. Fig. 2 shows the PCB stack-up. The thickness of the three dielectric layers from the top to bottom are 0.203 mm, 0.508 mm and 0.203 mm, respectively. RO 4450F prepreg ($\epsilon_r = 3.52, \tan\delta = 0.004$) of thickness 0.102 mm is used for bonding. The total height of the laminate is 1.12 mm. The 3rd metal layer (M3) is fully metalized and is used as the RF ground. It is worth mentioning that the potential impact of a large metallic display placed closely below the antennas is considered in the design process, which is a unique feature that previously reported studies have ignored.

A. DUAL-BAND HORIZONTALLY POLARIZED FOLDED DIPOLE

The planar half-wavelength dipole is by far the most popular choice for the realization of horizontally polarized fan-beam radiation in the endfire direction. We adopted the idea of the planar dipole but used a folded configuration to enhance the bandwidth in the 28 GHz band. The initial length of the folded dipole L_d is chosen to be around half of the wavelength at 28 GHz to create desired resonant response. The bandwidth is achieved by collectively adjusting the widths

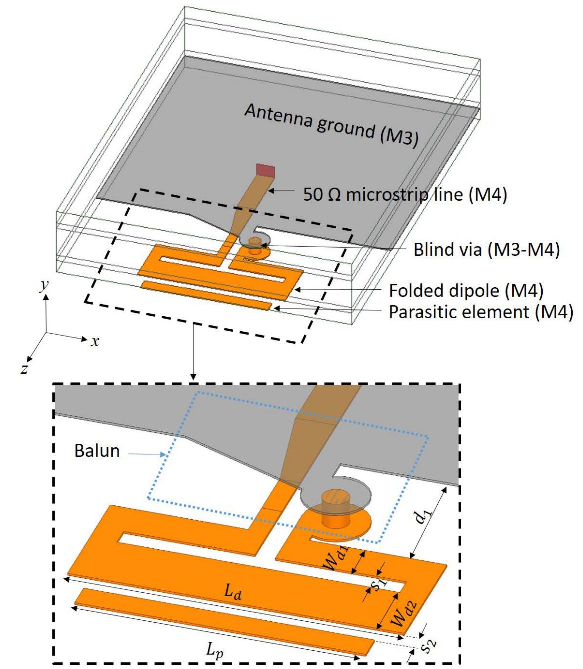

FIGURE 3. **Dual-band folded dipole with the balun. $L_d = 2.5$ mm, $L_p = 2.16$ mm, $W_{d1} = 0.3$ mm, $W_{d2} = 0.5$ mm, $s_1 = 0.15$ mm, $s_2 = 0.15$ mm, $d_1 = 0.7$ mm.**

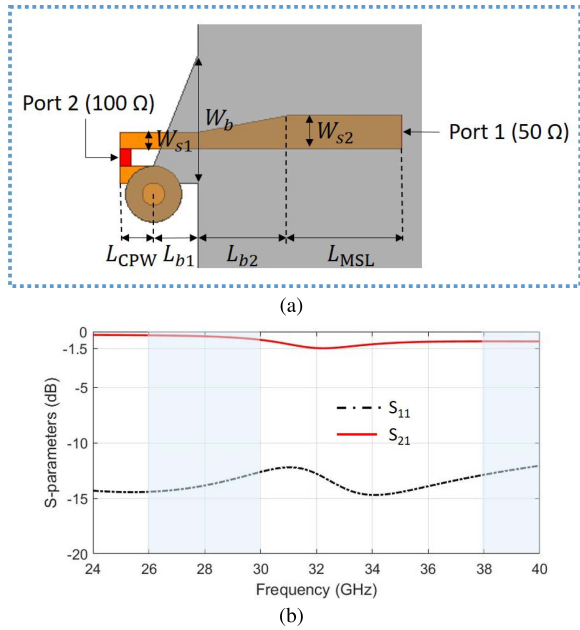

FIGURE 4. **(a) The coplanar-stripline-to-microstrip-line balun. $W_{s1} = 0.15$ mm, $W_{s2} = 0.3$ mm, $W_b = 1.15$ mm, $L_{b1} = 0.4$ mm, $L_{b2} = 0.8$ mm, $L_{CPW} = 0.3$ mm, $L_{MSL} = 1$ mm. (b) S-parameters of the balun.**

of the dipole W_{d1} and its folded arm W_{d2}, as well as the spacing s_1 in between. To realize the operation in the 39 GHz band, a parasitic strip is added in front of the driven element. The capacitive coupling between the folded dipole and the strip creates a resonance around 39 GHz. The addition of the parasitic strip also changes the response in the lower band, therefore, iterative parametric tuning is carried out to simultaneously match the antenna in both bands. The geometry of the antenna along with its design parameters is shown in Fig. 3. The antenna is configured on M4, and the reference ground is located on M3. The portion of the ground plane right above the antenna is removed so that the antenna can achieve desired matching performance. As the diffraction from the ground edge affects the radiation pattern of the antenna, the distance between the antenna and the edge of the ground plane d_1 is optimized for the maximum realized gain in the endfire direction.

Since the antenna will be connected to the output of a single-ended radio frequency integrated circuit (RFIC), a wideband balun is implemented to provide the transition from the balanced coplanar stripline to the unbalanced microstrip line as well as 100 Ω-to-50 Ω impedance matching. The close-up view in Fig. 3 shows the coplanar-stripline-to-microstrip-line balun connected to the folded dipole. The ground is gradually tapered towards one leg of the coplanar stripline and then connected to it through a blined via. The other leg of the coplanar stripline is progressively widened while extending towards the ground plane, and eventually transforms into a 50 Ω mictrostrip line. Fig. 4 (a) shows the 2-port configuration of the balun and its design parameters.

The port impedance of Port 2 is set to 100 Ω, which is compatible with the folded dipole and most commercial differential circuits. Fig. 4 (b) shows the S-parameters of the balun. The balun features a very wide bandwidth with maximum insertion loss of 0.74 dB in the lower band (26–30 GHz) and 0.89 dB in the higher band (38–40 GHz).

B. DUAL-BAND VERTICALLY POLARIZED HEXAGONAL BRIDGE ANTENNA

Vertically polarized endfire radiation is usually realized by utilizing a vertical dipole or a monopole to support currents in the vertical direction. The ultra-thin substrates used in smartphones pose a tremendous challenge of supporting such structures. Conventional antenna miniaturization is usually achieved at the expense of bandwidth and efficiency [20]–[23]. In this section, a hexagonal bridge antenna is proposed for vertically polarized radiation. This novel antenna topology features a very low profile of 0.92 mm ($0.08\lambda_0$ at 28 GHz) and maintains less than −10 dB reflection coefficients from 26.63 GHz to above 32 GHz in the lower band and from 37.9 GHz to above 40 GHz in the higher band. It should be noted that we deliberately choose a structure that requires a large ground plane as the ground plane can isolate the antenna from the metallic display, leading to more robust performance.

The design procedure consists of a number of intermediate steps as illustrated in Fig. 5. First, a wide nearly half-wavelength microstrip line is used as the basis of the design. The portion exceeding the height profile h is folded into a strip parallel to the ground with the end shorted to the ground. This structure constitutes a short-circuited half-wavelength microstrip line resonator. The 180° phase

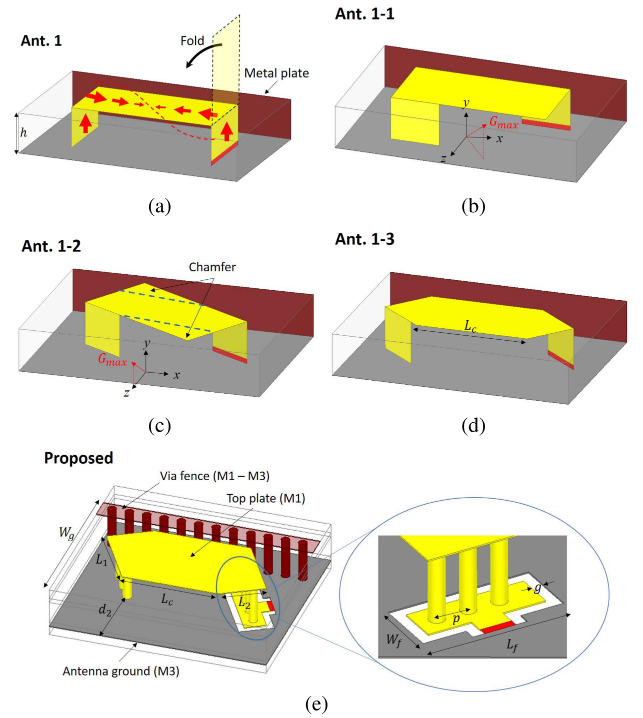

FIGURE 5. Design procedure of the dual-band vertically polarized hexagonal bridge antenna. (a) Fold a half-wavelength microstrip line. (b) Diagonally arrange the vertical plates. (c) Rotate the antenna. (d) Chamfer the corners. (e) The proposed antenna. $L_1 = 1.69$ mm, $L_c = 2.22$ mm, $L_2 = 1.07$ mm, $L_f = 1.8$ mm, $W_f = 0.8$ mm, $g = 0.15$ mm, $p = 0.4$ mm, $d_2 = 1.68$ mm, $W_g = 3.75$ mm.

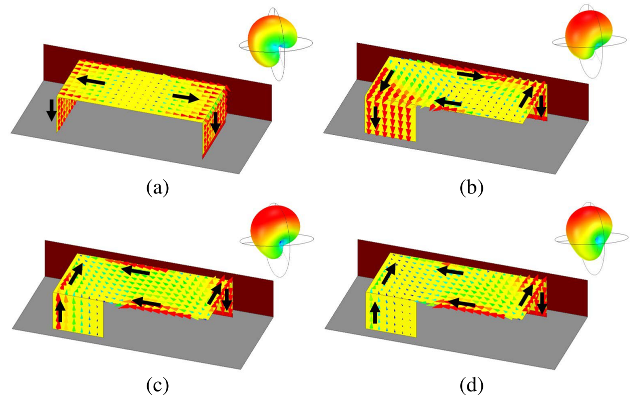

FIGURE 6. Current distribution and radiation patterns of (a) Ant.1 at 28 GHz, Ant.1-1 at (b) 26 GHz, (c) 28 GHz and (d) 30 GHz.

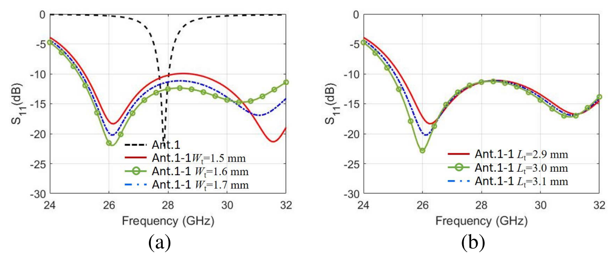

FIGURE 7. (a) Reflection coefficients of Ant.1 and Ant.1-1 with different W_t and fixed $L_t = 3$ mm. (b) Reflection coefficients of Ant.1-1 with different L_t and fixed $W_t = 1.6$ mm.

shift introduced by the half-wavelength transmission line results in the currents on the two vertical ends flowing in the same direction. These currents generate in-phase vertically polarized electric fields. Meanwhile, the horizontal current is canceled by its image on the ground plane. In addition, the horizontal current on the right side of the top plate is in the opposite direction of that on the left side, therefore unwanted horizontal radiation from these currents cancel each other in the far field as well, producing good polarization purity. A metal plate is added behind the antenna as a reflector to suppress the back radiation and isolate the antenna module from the RFICs.

Next, instead of placing the vertical plates on the left and right sides of the top plate, we place them diagonally along the front and back edges of the top plate as shown in Fig. 5 (b). This special arrangement allows the current to take different paths on the top plate, which leads to an additional resonance in the 28 GHz band. Fig. 6 (a)–(d) illustrate the current distribution and 3D radiation patterns of Ant.1 at 28 GHz, Ant.1-1 at 26 GHz, 28 GHz and 30 GHz, respectively. At 26 GHz, the current path length is around half the wavelength, and at 30 GHz, the current path length is slightly less than three quarters of the wavelength. Fig. 7 (a) compares the reflection coefficients of Ant.1 and Ant.1-1 from 24 GHz to 32 GHz. It is clear that Ant.1 only has one resonance with a very narrow bandwidth in the reported frequency range whereas Ant.1-1 has two wideband resonances. The influences of the width (W_t) and length (L_t) of the top plate on the reflection coefficients are investigated by varying one parameter with the other fixed. The results are shown in Fig. 7 (a) and (b), respectively. W_t has a much more significant impact on the higher resonance while L_t mainly controls the lower resonance, which indicates that bandwidth enhancement can be easily achieved by tuning the size of the top plate to merge the two resonances together. Furthermore, the radiation pattern of Ant.1-1 remains stable over the entire 28 GHz band.

However, the offset of the vertical plates in the z-direction causes the radiation pattern to rotate counterclockwise 35° about the y-axis. To compensate for this offset, the entire element is rotated 35° clockwise. Fig. 8 (a) shows the normalized radiation patterns in the xz-plane at 28 GHz before and after the rotation (Ant.1-1 and 1-2). The 3D radiation pattern of Ant.1-2 at 28 GHz is shown in Fig. 8 (b). The antenna features a quasi-endfire radiation pattern due to the finite ground plane. It provides maximum radiation at $\theta = 43°$ in the yz-plane and moderate radiation in the endfire direction.

For the high-band operation, the top plate is formed into a hexagon (Ant.1-3). The two open corners without the vertical plates are chamfered to create a full-wavelength current path at 39 GHz. Fig. 9 (a) illustrates the current distribution on the antenna at 39 GHz. The resonant frequency can be adjusted by changing the size of the chamfer L_c. Fig. 9 (b) shows the reflection coefficients of the antenna in the 39 GHz band for different chamfer sizes. For comparison, the reflection

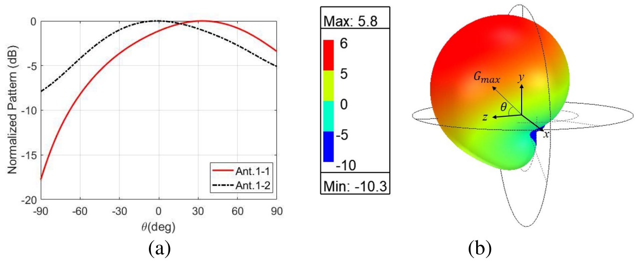

FIGURE 8. (a) Normalized radiation patterns of Ant.1-1 and Ant.1-2 in the xz-plane at 28 GHz. (b) 3D radiation pattern of Ant.1-2 at 28 GHz.

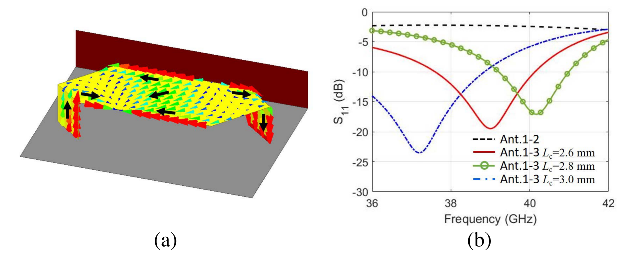

FIGURE 9. (a) Current distribution of Ant.1-3 at 39 GHz. (b) Reflection coefficients of Ant.1-3 for different chamfer sizes.

coefficients of the antenna without the chamfer (Ant.1-2) is also plotted in the figure. The resonance moves to lower frequencies as L_c increases. The final version of the vertically polarized hexagonal bridge antenna and its design parameters are presented in Fig. 5 (e). The structure is implemented between M1 and M3. The vertical plates and the reflector are realized by closely spaced blind vias with a diameter of 0.2 mm. Spacing of 0.4 mm between adjacent vias is found sufficient. The feed vias are connected together by a rectangular pad on M3 and are fed using a coplanar waveguide. The distance from the antenna to the edge of the ground plane d_2 is adjusted for the best radiation performance while minimizing the width of the ground W_g.

C. DUAL-BAND DUAL-POLARIZED ARRAY ELEMENT

The two antennas are combined into a dual-band dual-polarized array element as shown in Fig. 10. The folded dipole is placed at the edge of the PCB with the hexagonal bridge antenna located behind it. Although this configuration has a slightly larger dimension along the z-axis compared with the side-by-side configuration, it significantly reduces the footprint along the x-axis, and has a better scanning capability when forming an array. The total size of the array element is 6.5 mm × 5 mm × 1.12 mm.

The impact of a metallic display on antenna input impedance is also investigated. The reflection coefficients of the horizontally polarized (H-pol) and vertically polarized (V-pol) antennas for different display distance d are plotted in Fig. 11 (a) and (b), respectively. Thanks to the ground plane, the V-pol antenna is only slightly affected by the display and has a good matching performance even when the display is placed as close as 1 mm. The H-pol antenna is more vulnerable to the position of the display since there is no ground plane to shield the antenna. Nevertheless, it is well matched when the display is placed more than 3 mm away from the bottom of the substrate. Considering that the typical thickness of smartphones is about 7.5 mm − 10 mm [24], a distance of 3 − 5 mm is adequate for most smartphone manufacturers. If a smaller distance is desired, the H-pol antenna can be optimized for that specific distance.

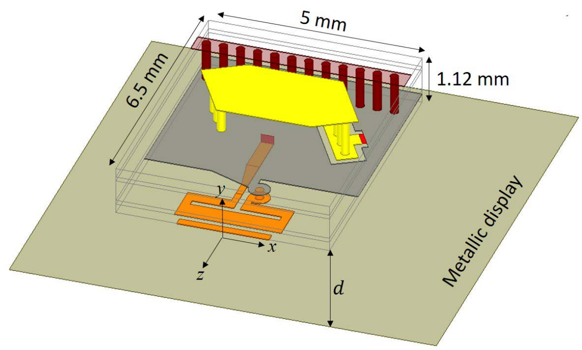

FIGURE 10. The proposed dual-band dual-polarized array element.

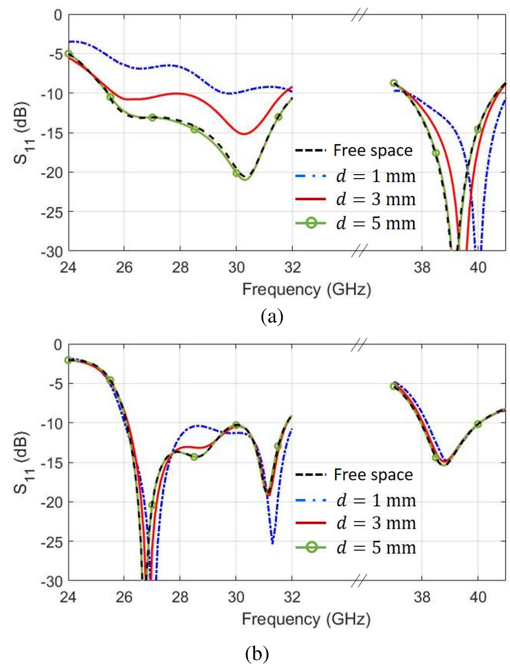

FIGURE 11. Reflection coefficients of the (a) H-pol and (b) V-pol antennas for different display distances.

III. ANTENNA MEASUREMENTS

Since the signal lines of the H-pol antenna and the V-pol antenna are located on M4 and M3, respectively, it is impractical to directly characterize the antennas using a RF probe-based setup. In order to excite the H-pol antenna with a RF probe from M1, the microstrip line on M4 is elongated to the

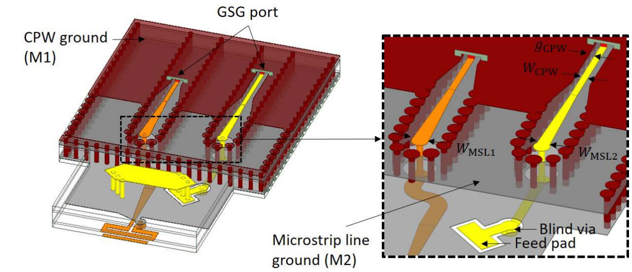

FIGURE 12. The proposed array element with the GSG probe feeding network. W_{CPW} = 0.2 mm, g_{CPW} = 0.18 mm, W_{MSL1} = 0.5 mm, W_{MSL2} = 0.4 mm.

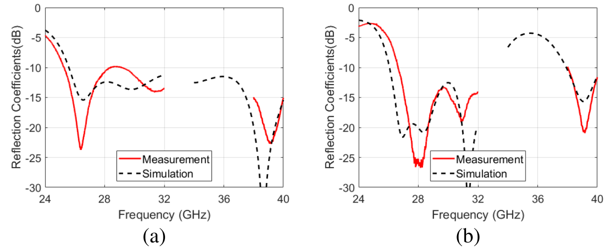

FIGURE 13. Reflection coefficients of the (a) H-pol and (b) V-pol antennas.

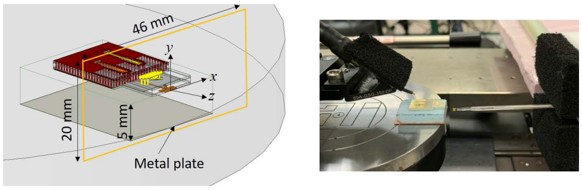

FIGURE 14. Near-field scan configuration.

back of the via-fence and then connected to M1 through a vertical through via. A small circular incision is made on the ground plane for the signal via to pass through. A grounded coplanar waveguide (GCPW) to microstrip line transition is implemented on M1 to route the signal from the ground-signal-ground (GSG) probe to the via interconnect. The reference ground of the microstrip line (which is also the bottom ground of the GCPW) is configured on M2. The final configuration of the antenna with the GSG probe feeding network is shown in Fig. 12. It should be noted that the feeding network is only for testing purposes and is not considered part of the antenna. The close-up view shows the details of the transition from the original ports to the GSG ports. The width of the center signal line W_{CPW} and the gap between the signal line and the ground g_{CPW} at the probe end is predetermined by the tip size and pitch of the GSG RF probe. The gap is gradually widened to ensure a smooth transition of the electric field from the GCPW to the microstrip line. The tapered microstrip line is matched to 50 Ω. The three ground planes (i.e., the CPW ground on M1, the micrstrip line ground on M2, and the antenna ground on M3) are electrically connected by a series through vias surrounding the transmission line and the via at the interconnect. The diameters of the vias and via pads are configured to be 0.2 mm and 0.5 mm, respectively. The vias not only serve the purpose of electrical connection, but also suppress unwanted parallel plate waveguide modes and surface waves. For the V-pol antenna, a similar GCPW to microstrip line transition using a combination of strip lines and through vias is implemented. The signal is first routed from the GSG probe to the microstrip line on M1, then passed to the micrstrip line on M4 through the interconnect via, and eventually fed into the antenna by a blind via that connects the end of the micrstrip line (M4) to the center signal line of the CPW on M3. The fabricated array element is shown in Fig. 19.

A GSG RF probe from GGB Industries (Picoprobe 50A-GSG-350-DP) and a network analyzer (Agilent 8722ES) are used to extract the reflection coefficients of the antennas. The system is calibrated to the probe tips using a standard calibration substrate (GGB Industries Inc. Model CS-9). The array element is suspended on a 5 mm thick Styrofoam layer. To include the impact of a metallic display in antenna characterization, a metal plate is added at the bottom of the supporting Styrofoam to mimic the display. During the measurement, only one port is excited at a time, with the other port terminated with a high-frequency 50 Ω resistor. The measured reflection coefficients of the H-pol and V-pol antennas are plotted in Fig. 13 (a) and (b), respectively, and are compared with the simulated results. The measurement is overall in good agreement with the simulation. Both antennas achieve the desired bandwidth. The discrepancies are attributed to the fabrication errors, particularly, the thickness of the prepreg bonding layer, the diameter of the via holes and the spacing between adjacent vias. It should be mentioned that the simulated reflection coefficients in Fig. 13 are slightly different from those in Fig. 11. This is because the measured and simulated reflection coefficients in Fig. 13 include the GSG probe feeding network whereas the results in Fig. 11 are obtained without the feeding network.

The radiation patterns of the antennas are characterized using the near-field to far-field (NF/FF) method. An electro-optic (EO) near-field scan system, NeoScan [25], is used to map the near-fields of the antennas. The scan configuration is illustrated in Fig. 14. The scan plane is 1 mm away from the edge of the antenna. The scan area is set to 46 mm × 20 mm and the sampling resolution is 0.5 mm. The measured near field distribution of the H-pol and V-pol antennas at 28 GHz and 39 GHz are presented in Fig. 15 (a)–(d), respectively. The corresponding normalized far-field radiation patterns in the *xz*- and *yz*-planes are plotted in Fig. 16 in conjunction with the simulated patterns. Since the cross-polarized signal level is below the sensitivity of the near-field scan system, we are unable to accurately measure the cross-polarized radiation. However, this also proves that the antennas have good polarization purity.

In general, the measured co-polarized patterns are in good agreement with the simulated ones. The discrepancies mainly stem from the finite size of the scan area. As expected,

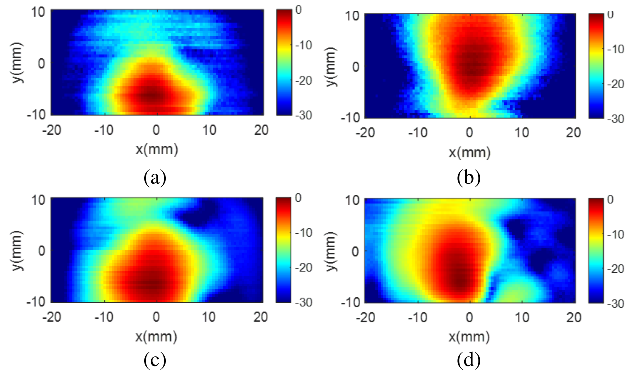

FIGURE 15. Near-field distribution of (a) H-pol and (b) V-pol antennas at 28 GHz; (c) H-pol and (d) V-pol antennas at 39 GHz.

the measured patterns diverge from the simulated results for large angles. This issue is more sever in the *yz*-plane than that in the *xz*-plane, especially for the V-pol antenna because of the limited measurable range in the *y*-direction (maximum 20 mm). The ripples in the measured patterns are due to the abrupt truncation of the scan plane. The H-pol antenna provides excellent endfire radiation at both 28 GHz and 39 GHz. The V-pol antenna produces a quasi-endfire radiation pattern at 28 GHz. At 39 GHz, the maximum V-pol radiation slightly shifts toward the $-x$ direction. This is due to the phase differences of the currents on the vertical vias at 39 GHz. Another point worth noting is that, the simulated 39 GHz patterns have some ripples in the *yz*-plane for $\theta > 60°$. After careful investigation, it is found that the ripples are caused by the edge diffraction from the metallic display underneath the antenna. This phenomenon is not captured by the measurement due to the limited scanning capability.

The absolute gains of the antennas in the endfire direction (along $+z$) are obtained using the image method [26] and are plotted in Fig. 17 (a)–(d), respectively. The gains are relatively flat in the two operating bands, indicating consistent radiation performance over the entire bands. The gains at 28 and 39 GHz are summarized in Table 1. The measured results agree well with the simulated ones. The peak gains are then determined based on the radiation patterns in the *yz*-plane. Due to limited measurement capability, we are not able to obtain the maximum radiation of the V-pol antenna in the *yz*-plane, therefore only simulated peak gains of the V-pol antenna are reported. Considering the good agreement in all other measurements, we believe that the simulated results are accurate.

IV. PHASED ARRAY DESIGN

The array element is expanded into a 1×4 phased array as shown in Fig. 18. The array is symmetric about the center line (dotted orange line). The inter-element spacing is set to 6 mm ($0.56\lambda_0$ at 28 GHz, $0.78\lambda_0$ at 39 GHz) to achieve a minimum of 10 dB port-to-port isolation in the 28 GHz band. The overall real estate of the array is 6.5 mm $\times$ 23 mm $\times$ 1.12 mm excluding the feeding network behind the via fence. Fig. 19 shows the fabricated array.

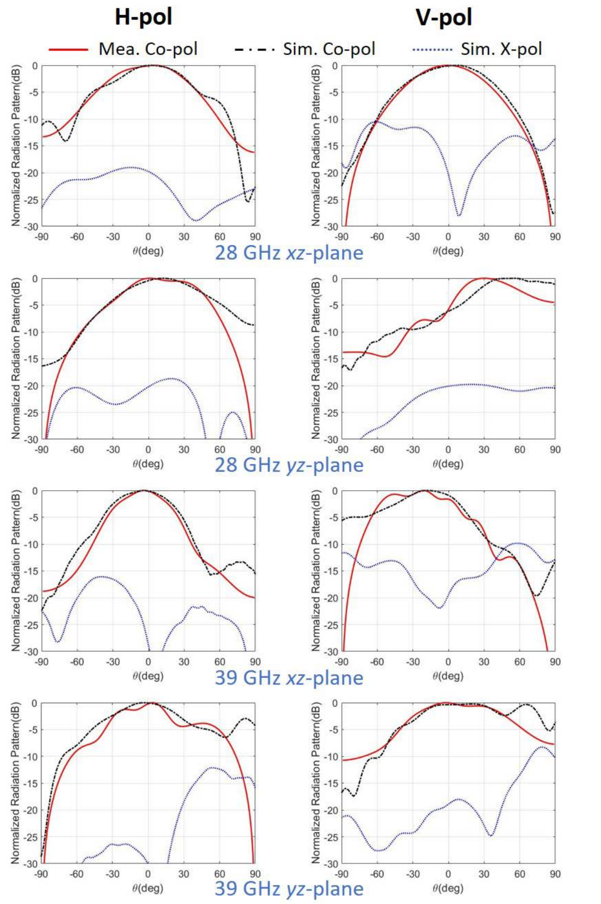

FIGURE 16. Far-field radiation patterns of H-pol and V-pol antennas in *xz*- and *yz*-planes at 28 GHz and 39 GHz.

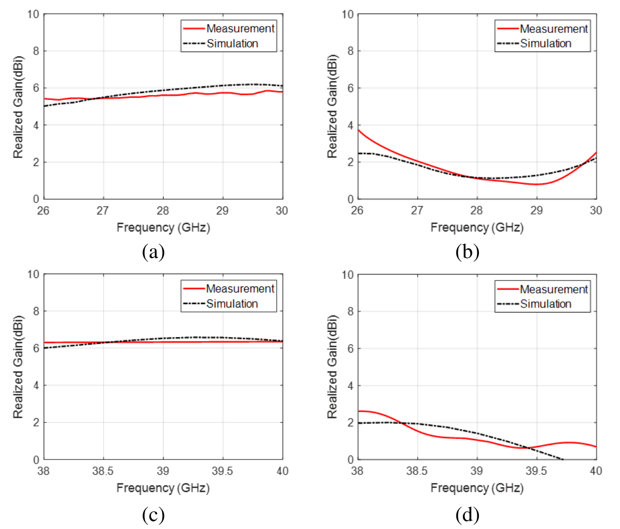

FIGURE 17. Absolute gains of the antennas in the endfire direction. (a) H-pol and (b) V-pol antennas in the 28 GHz band; (c) H-pol and (d) V-pol antennas in the 39 GHz band.

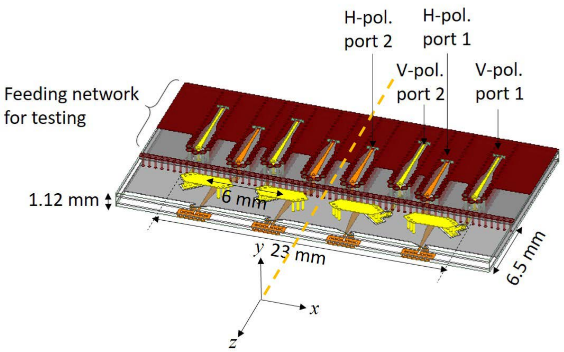

FIGURE 18. The proposed 1 × 4 phased array with the GSG probe feeding network. Array port numbering from the right to the left: port 1-4.

TABLE 1. Absolute gains of the array element (Unit: dBi).

	28 GHz		39 GHz	
	H-pol	V-pol	H-pol	V-pol
Endfire Meas.	5.59	1.16	6.33	1.11
Endfire Simu.	5.88	1.15	6.53	1.42
Peak Meas.	5.59	-	6.51	-
Peak Simu.	6.15	5.95	7.02	6.91

The reflection coefficients of each element are measured using the GSG RF probe with other 7 ports terminated with 50 Ω resistors. Only 4 ports (H-pol port 1 and 2, V-pol port 1 and 2) need to be measured due to the symmetry of the array. The measured reflection coefficients are plotted in conjunction with the simulated results in Fig. 20. Less than −10 dB reflection is achieved in the desired 26–30 GHz and 38–40 GHz bands. The center frequencies of V-pol port 1 and 4 slightly shift down in the high band. The V-pol antennas are found to be more susceptible to fabrication errors than the H-pol antennas because of the extensive use of blind vias in the structure. The port-to-port couplings between elements are plotted in Fig. 21. Due to the close spacing between the ports, we are unable to land two RF probes simultaneously to measure the couplings, therefore, only simulated results are reported. For the clarity of the figure, only four pairs of ports with the highest couplings are presented in each band. The couplings are less than −13.89 dB in the lower band and less than −20.65 in the higher band.

The radiation patterns of the array are also obtained using the NF/FF method. A metal plate is again placed 5 mm below the array to emulate a metallic display. We measure the near-field of each element (with other elements terminated with 50 Ω resistors), and the total near-field of the H-pol (V-pol) array is formed from the superposition of the measured near-fields of the H-pol (V-pol) elements. The total near-fields of the H-pol and the V-pol arrays with uniform excitation at 28 GHz and 39 GHz are shown in Fig. 22 (a)–(d), and the normalized far-field patterns in the *xz*- and *yz*-planes are plotted in Fig. 23, along with the simulated results. As desired, the H-pol array provides an

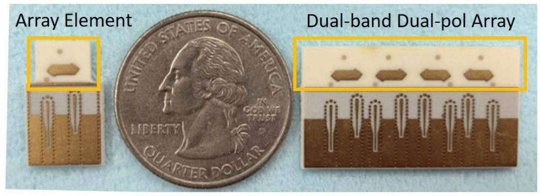

FIGURE 19. The fabricated dual-band dual-polarized array element and the full array.

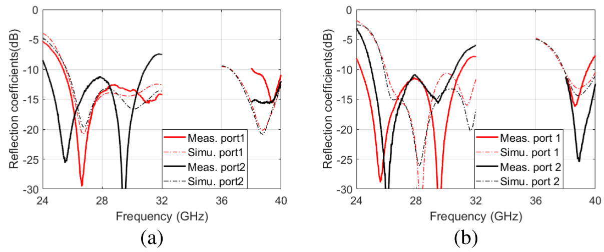

FIGURE 20. Reflection coefficients of the phased arrays. (a) H-pol port 1 and 2. (b) V-pol port 1 and 2.

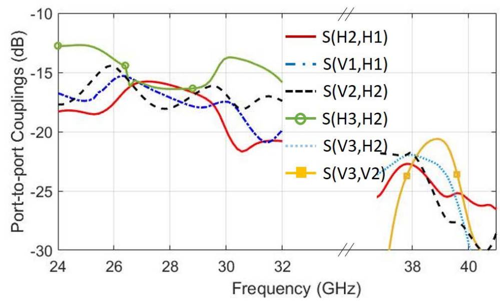

FIGURE 21. Port-to-port couplings between elements.

endfire radiation pattern while the V-pol array provides a quasi-endfire radiation pattern. The main beams of the array in the *xz*-plane are in excellent agreement with the simulated results, and the deviations of the first sidelobe level are within 2.5 dB. Similar to the single element measurement, the patterns diverge from the simulation for large angles due to the finite scan area, and the issue is more sever in the *yz*-plane for the V-pol array. Unlike the single element patterns, all array patterns are completely symmetric in the *xz*-plane owing to the symmetric arrangement of the elements. It should be noted that the cross-polarized radiation in the *yz*-plane is more than 50 dB below the co-polarized radiation level, therefore, it is not shown in the figures.

The gains of the arrays are characterized using the NF/FF gain comparison method [26]. We choose the array element as the standard gain antenna, and use the measured gains listed in Table 1 in the calculations. The complete array gains for both polarizations at 28 GHz and 39 GHz are tabulated in Table 2 in conjunction with the simulated gains. The measured gains agree well with the simulation. Similar to the single array element, we are not able to accurately obtain

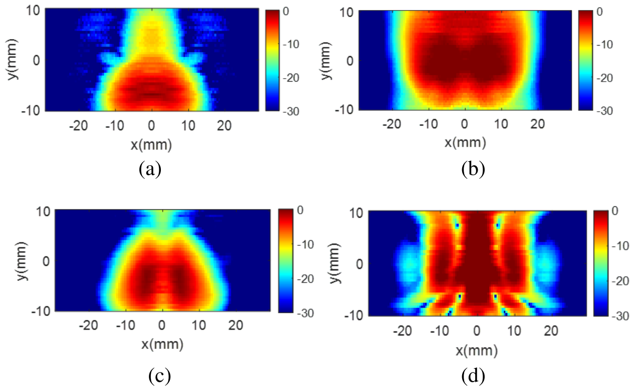

FIGURE 22. Near-field distribution of (a) H-pol and (b) V-pol arrays at 28 GHz; (c) H-pol and (d) V-pol arrays at 39 GHz.

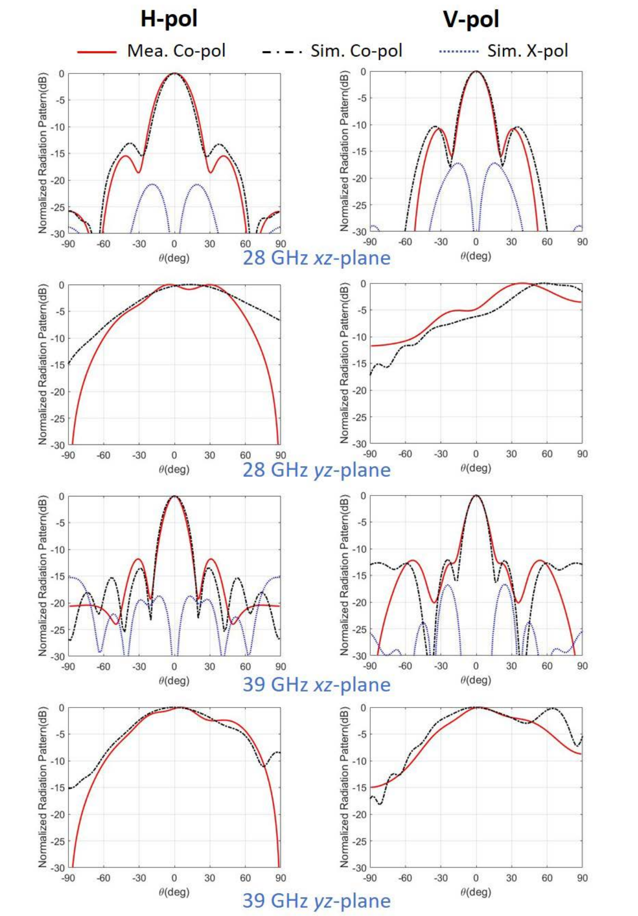

FIGURE 23. Far-field radiation patterns of the H-pol and V-pol arrays in the *xz*- and *yz*-planes at 28 GHz and 39 GHz.

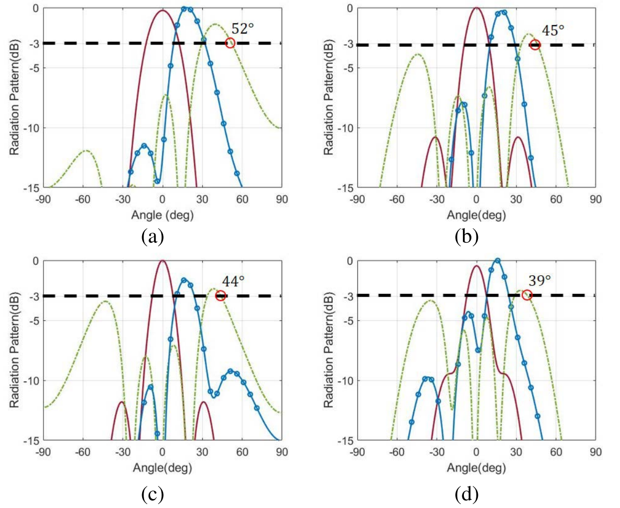

FIGURE 24. Scan performance of the array. (a) H-pol and (b) V-pol arrays at 28 GHz; (c) H-pol and (d) V-pol arrays at 39 GHz.

TABLE 2. Absolute gains of the array with uniform excitation (Unit: dBi).

	28 GHz		39 GHz	
	H-pol	V-pol	H-pol	V-pol
Endfire Meas.	11.05	5.55	11.7	6.65
Endfire Simu.	10.15	5.47	10.93	6.96
Peak Meas.	11.31	-	11.93	-
Peak Simu.	10.41	11.71	11.29	12.42

the peak gains of the V-pol array, therefore, only simulated peak gains are presented.

The scan performance of the array is demonstrated in Fig. 24. The overlapped 3 dB scan ranges between both polarizations are ±45° at 28 GHz and ±39° at 39 GHz. The smaller scan range at 39 GHz can be explained by noting that the maximum scan angle θ_m without grating lobes is related to the inter-element spacing d_e by [27]

$$d_e < \frac{\lambda_0}{1 + |\cos\theta_m|} \tag{1}$$

Since the inter-element spacing is larger in terms of wavelength at higher frequencies, grating lobes start to appear at smaller scan angles at 39 GHz. The different scan ranges of the H-pol and V-pol arrays at the same frequency are attributed to the difference in array element pattern. However, it should be mentioned that, for 5G communications, grating lobes are not critical as long as the gain and spatial coverage align with the specifications [19], [28]. This is different from radar applications where the presence of grating lobes or large sidelobes is undesired. In fact, for 5G applications, grating lobes may even help enlarge the spatial coverage [28]. The overall influence of grating lobes on mmWave communication still needs more investigation.

In Table 3, the key characteristics of the proposed array are listed and compared with some recently reported dual-band dual-polarized 5G mmWave arrays. As clearly shown in the table, the proposed array outperforms most of the existing solutions in terms of height profile and average size of the array element (i.e., total size/number of array elements). More importantly, [6], [7], [10]–[12] are all broadside antenna arrays. They do not provide the same coverage, nor do they face the same design challenges as endfire arrays, especially for the realization of vertically polarized radiation

TABLE 3. Performance comparison of recent dual-band dual-polarized 5G mmWave antenna arrays.

Ref.	Array Configuration	Size Total / Per Element (λ_L^{3*}) ($l \times w \times h$)	Bandwidth (GHz)	Max. Scan Angle**	Peak Gain (dBi) H-pol/V-pol
[6] (Simulation)	1×8 Broadside	0.15 / 0.018 ($4.38 \times 0.93 \times 0.04$)	27.9–28.3 38.6–39.3	53° @ 28 GHz 50° @ 39 GHz	15.2 / 15.2 @ 28 GHz 16.9 / 15.0 @ 39 GHz
[7]	2×2 Broadside	0.49 / 0.124 ($1.61 \times 1.61 \times 0.19$)	24.2–27.8 36.9–42.8	N.A.	13.3 / 13.3 @ 26 GHz 15.6 / 15.0 @ 39 GHz
[10]	2×2 Broadside	0.26 / 0.066 ($1.28 \times 1.28 \times 0.16$)	23.3–31.7 42.5–46.5	51° @ 27 GHz 31° @ 45 GHz	11.0 / 11.0 @ 27 GHz 12.5 / 12.5 @ 45 GHz
[11]	1×4 Broadside	0.06 / 0.016 ($1.67 \times 0.38 \times 0.10$)	26.2–29.6 35.2–41.0	60° @ 28 GHz 25° @ 39 GHz	10.5 / 10.2 @ 28 GHz 11.9 / 10.8 @ 39 GHz
[12]	2×2 Broadside	3.47 / 0.867 ($3.08 \times 3.26 \times 0.34$)	27.2–30.2 35.7–40.3	18° @ 28 GHz 44° @ 38 GHz	13.2 / 9.5 @ 28 GHz 10.5 / 13.2 @ 38 GHz
[19]	1×8 Quasi-endfire	0.28 / 0.035 ($4.93 \times 0.40 \times 0.14$)	27.1–39.5	75° @ 28 GHz 44° @ 38 GHz	10.5 / 11.6 @ 28 GHz 13.0 / 10.0 @ 45 GHz
This work	**1×4 Quasi-endfire**	**0.10 / 0.025 ($1.95 \times 0.55 \times 0.09$)**	**25.4–30.8 38.0–40.0**	**52° @ 28 GHz 44° @ 39 GHz**	**11.1 / 11.7 @ 28 GHz 11.9 / 12.4 @ 45 GHz**

*λ_L is the free-space wavelength at the lowest operating frequency.
**In the literature, the maximum scan angle is defined in terms of the 3 dB scan range of the H-pol or V-pol array (whichever is larger).

in very thin substrates. Compared with the quasi-endfire array reported in [19], this work can provide similar H-pol peak gain and higher V-pol peak gain with only half the number of elements. Since [19] only reports the scan performance of the H-pol array, we are unable to compare the overlapped scan range between both polarizations.

V. CONCLUSION

A highly compact dual-band dual-polarized antenna array for 5G smartphones is designed, analyzed and discussed. The array utilizes a pair of antennas to provide two orthogonal linear polarizations in both the 28 GHz and 39 GHz bands designated for 5G uses. A great advantage of this design is that it can be directly integrated with cellphone PCBs, offering a low-cost solution to mmWave 5G antennas for cellular devices.

ACKNOWLEDGMENT

The authors would like to thank Qualcomm for their support of this work. The NeoScan system used in the measurement is commercialized by EMAG Technologies in which Prof. Sarabandi is a principal.

REFERENCES

[1] Z. Pi and F. Khan, "An introduction to millimeter-wave mobile broadband systems," *IEEE Commun. Mag.*, vol. 49, no. 6, pp. 101–107, Jun. 2011.
[2] T. S. Rappaport, S. Sun, R. Mayzus, H. Zhao, Y. Azar, K. Wang, G. N. Wong, J. K. Schulz, M. Samimi, and F. Gutierrez, "Millimeter wave mobile communications for 5G cellular: It will work!" *IEEE Access*, vol. 1, pp. 335–349, 2013.
[3] *America's 5G Future*. Accessed: Jan. 2022. [Online]. Available: https://www.fcc.gov/5G
[4] W. Hong, K. Baek, and Y. Lee, "Quantitative analysis of the effects of polarization and pattern reconfiguration for mmWave 5G mobile antenna prototypes," in *Proc. IEEE Radio Wireless Symp. (RWS)*, Jan. 2017, pp. 68–71.
[5] W. Hong, K.-H. Baek, and S. Ko, "Millimeter-wave 5G antennas for smartphones: Overview and experimental demonstration," *IEEE Trans. Antennas Propag.*, vol. 65, no. 12, pp. 6250–6261, Dec. 2017.
[6] S. Lee, S. Kim, and J. Choi, "Dual-band dual-polarized proximity fed patch antenna for 28 GHz/39 GHz 5G millimeter-wave communications," in *Proc. 13th Eur. Conf. Antennas Propag. (EuCAP)*, 2019, pp. 1–5.
[7] B. Feng, X. He, J. Cheng, and C. Sim, "Dual-wideband dual-polarized metasurface antenna array for the 5G millimeter wave communications based on characteristic mode theory," *IEEE Access*, vol. 8, pp. 21589–21601, 2020.
[8] Y. He, M. Rao, Y. Liu, G. Jing, M. Xi, and L. Zhao, "28/39-GHz dual-band dual-polarized millimeter wave stacked patch antenna array for 5G applications," in *Proc. Int. Workshop Antenna Technol. (iWAT)*, Feb. 2020, pp. 1–4.
[9] Z. Siddiqui, M. Sonkki, J. Chen, M. Berg, M. E. Leinonen, and A. Pärssinen, "Dual-band dual-polarized antenna for mm-wave 5G base station antenna array," in *Proc. 14th Eur. Conf. Antennas Propag. (EuCAP)*, Mar. 2020, pp. 1–4.
[10] W. Sun, Y. Li, L. Chang, H. Li, X. Qin, and H. Wang, "Dual-band dual-polarized microstrip antenna array using double-layer gridded patches for 5G millimeter-wave applications," *IEEE Trans. Antennas Propag.*, vol. 69, no. 10, pp. 6489–6499, Oct. 2021.
[11] J. Seo, I. Yoon, J. Jung, J. Ryoo, J. Park, W. Lee, D. Ko, and J. Oh, "Miniaturized dual-band broadside/endfire antenna-in-package for 5G smartphone," *IEEE Trans. Antennas Propag.*, vol. 69, no. 12, pp. 8100–8114, Dec. 2021.
[12] H.-N. Hu, F.-P. Lai, and Y.-S. Chen, "Dual-band dual-polarized scalable antenna subarray for compact millimeter-wave 5G base stations," *IEEE Access*, vol. 8, pp. 129180–129192, 2020.
[13] N. O. Parchin, M. Shen, and G. F. Pedersen, "End-fire phased array 5G antenna design using leaf-shaped bow-tie elements for 28/38 GHz MIMO applications," in *Proc. IEEE Int. Conf. Ubiquitous Wireless Broadband (ICUWB)*, Oct. 2016, pp. 1–4.
[14] W. Hong, S.-T. Ko, Y. Lee, and K.-H. Baek, "Compact 28 GHz antenna array with full polarization flexibility under yaw, pitch, roll motions," in *Proc. 9th Eur. Conf. Antennas Propag. (EuCAP)*, 2015, pp. 1–3.
[15] W. El-Halwagy, R. Mirzavand, J. Melzer, M. Hossain, and P. Mousavi, "Investigation of wideband substrate-integrated vertically-polarized electric dipole antenna and arrays for mm-wave 5G mobile devices," *IEEE Access*, vol. 6, pp. 2145–2157, 2018.
[16] J. Park, D. Choi, and W. Hong, "37–39 GHz vertically-polarized end-fire 5G antenna array featuring electrically small profile," in *Proc. IEEE Int. Symp. Antennas Propag., USNC/URSI Nat. Radio Sci. Meeting*, Jul. 2018, pp. 637–638.
[17] R. M. Moreno, J. Ala-Laurinaho, A. Khripkov, J. Ilvonen, and V. Viikari, "Dual-polarized mm-wave endfire antenna for mobile devices," *IEEE Trans. Antennas Propag.*, vol. 68, no. 8, pp. 5924–5934, Aug. 2020.
[18] R. Lu, C. Yu, Y. Zhu, and W. Hong, "Compact millimeter-wave endfire dual-polarized antenna array for low-cost multibeam applications," *IEEE Antennas Wireless Propag. Lett.*, vol. 19, no. 12, pp. 2526–2530, Dec. 2020.
[19] N. O. Parchin, J. Zhang, R. A. Abd-Alhameed, G. F. Pedersen, and S. Zhang, "A planar dual-polarized phased array with broad bandwidth and quasi-endfire radiation for 5G mobile handsets," *IEEE Trans. Antennas Propag.*, vol. 69, no. 10, pp. 6410–6419, Oct. 2021.
[20] W. Hong and K. Sarabandi, "Low profile miniaturized planar antenna with omnidirectional vertically polarized radiation," *IEEE Trans. Antennas Propag.*, vol. 56, no. 6, pp. 1533–1540, Jun. 2008.
[21] W. Hong and K. Sarabandi, "Low-profile, multi-element, miniaturized monopole antenna," *IEEE Trans. Antennas Propag.*, vol. 57, no. 1, pp. 72–80, Jan. 2009.

[22] J. Oh and K. Sarabandi, ''Low profile, miniaturized, inductively coupled capacitively loaded monopole antenna,'' *IEEE Trans. Antennas Propag.*, vol. 60, no. 3, pp. 1206–1213, Mar. 2012.

[23] J. Oh and K. Sarabandi, ''Low profile vertically polarized omnidirectional wideband antenna with capacitively coupled parasitic elements,'' *IEEE Trans. Antennas Propag.*, vol. 62, no. 2, pp. 977–982, Feb. 2014.

[24] S. Ratnaker. (2021). *Mobile Phone Size Comparison—Complete Guide*. [Online]. Available: https://inventionofmobilephones.com/mobile-phone-size-comparison-complete-guide/

[25] *Neoscan*. Accessed: Jan. 2022. [Online]. Available: https://neoscan.com

[26] M. Rao and K. Sarabandi, ''A near-field-based gain and pattern measurement technique for probe-fed millimeter-wave antennas,'' 2021.

[27] W. L. Stutzman and G. A. Thiele, *Antenna Theory and Design*, 3rd ed. Hoboken, NJ, USA: Wiley, 2004.

[28] K. Zhao, S. Zhang, Z. Ho, O. Zander, T. Bolin, Z. Ying, and G. F. Pedersen, ''Spherical coverage characterization of 5G millimeter wave user equipment with 3GPP specifications,'' *IEEE Access*, vol. 7, pp. 4442–4452, 2019.

MENGLOU RAO (Graduate Student Member, IEEE) received the B.Eng. degree in electrical engineering from the Beijing University of Posts and Telecommunications, Beijing, China, in 2016. She is currently pursuing the Ph.D. degree in electrical engineering with the University of Michigan, Ann Arbor, MI, USA. She has been with the Radiation Laboratory, Department of Electrical Engineering and Computer Science, University of Michigan, as a Graduate Research Assistant, since 2017. Her research interests include miniaturized antennas, mm-Wave antenna design, and measurements.

KAMAL SARABANDI (Life Fellow, IEEE) is currently the Rufus S. Teesdale Endowed Professor in engineering with the University of Michigan. He has supervised 59 Ph.D. and numerous master's students and postdoctoral fellows. He has published many book chapters, more than 315 articles in refereed journals, and more than 760 conference papers. He, together with his students, are recipients of 35 paper awards. His research interests include microwave and millimeter-wave radar remote sensing, meta-materials, electromagnetic wave propagation, and antenna miniaturization. He served as a member for NASA Advisory Council for two consecutive terms, from 2006 to 2010, and served as the President for the IEEE Geoscience and Remote Sensing Society (2015–2016). He is the Past Chair of the Commission F of USNC/URSI and serving as a member for the AdCom for the IEEE Antennas and Propagation Society. He led the Center for Microelectronics and Sensors funded by the Army Research Laboratory (2008–2018) and is leading the Center of Excellence in Microwave Sensor Technology. His contributions to the field of electromagnetics have been recognized by many awards, including Humboldt Research Award, the IEEE GRSS Distinguished Achievement Award, the IEEE Judith A. Resnik Medal, the IEEE GRSS Education Award, NASA Group Achievement Award, and many other wards from the University of Michigan. He is a fellow of the American Association for the Advancement of Science (AAAS) and a fellow of the National Academy of Inventors. He is a member of the National Academy of Engineering.